Copper delocalization leads to ultralow thermal conductivity in chalcohalide $CuBiSeCl_2$

Yuzhou Hao,[1] Junwei Che,[2] Xiaoying Wang,[1] Xuejie Li,[1] Turab Lookman,[3] Jun Sun,[1] Xiangdong Ding,[1] and Zhibin Gao[1,*]

[1]*State Key Laboratory for Mechanical Behavior of Materials, School of Materials Science and Engineering, Xi'an Jiaotong University, Xi'an 710049, China*

[2]*Department of Applied Physics, Xi'an University of Science and Technology, Xi'an 710054, China*

[3]*AiMaterials Research LLC, Santa Fe, New Mexico 87501, USA*

(Received 1 January 2025; revised 9 April 2025; accepted 28 April 2025; published 13 May 2025)

Mixed anion halide-chalcogenide materials have attracted considerable attention due to their exceptional optoelectronic properties, making them promising candidates for various applications. Among these, $CuBiSeCl_2$ has recently been experimentally identified with remarkably low lattice thermal conductivity (κ_L). In this study, we employ Wigner transport theory combined with neuroevolution machine learning potential-assisted self-consistent phonon calculations to unravel the microscopic origins of this low κ_L. Our findings reveal that the delocalization and weak bonding of copper atoms are key contributors to the strong phonon anharmonicity and wavelike tunneling (random walk diffusons). These insights deepen our understanding of the relationship between bonding characteristics, anharmonicity, delocalization, and vibrational dynamics, paving the way for the design and optimization of $CuBiSeCl_2$ and analogous materials for advanced phonon engineering applications.

DOI: 10.1103/PhysRevB.111.195207

I. INTRODUCTION

Mixed-anion compounds, such as halide-chalcogenides, have recently gained attention as promising candidates for thermoelectric and photovoltaic applications due to their ability to achieve low thermal conductivity while maintaining favorable electronic properties [1–3]. These compounds exhibit increased structural anisotropy, dimensional changes, and the formation of novel structural types [4]. The structural modifications induced by variations in bonding promote the emergence of new physical phenomena and offer opportunities to tune both optoelectronic and thermoelectronic properties by altering the electronic structure [5–9].

$CuBiSeCl_2$, a mixed-metal chalcohalide, stands out for its potential to exhibit both low thermal conductivity and favorable electronic properties. Previous experimental studies have shown that $CuBiSeCl_2$ has a band gap of 1.33 eV, as measured by diffuse reflectance UV-vis spectroscopy, making it suitable for photovoltaic applications [4]. Additionally, it demonstrates a low thermal conductivity of 0.27 W m^{-1} K^{-1} at room temperature [4]. However, the complex crystal structure has limited comprehensive studies on the underlying mechanisms responsible for its low κ_L, particularly for such intricate mixed-anion compounds.

In this study, we investigate the microscopic mechanisms underlying the low κ_L of $CuBiSeCl_2$ by combining machine learning potentials with anharmonic lattice dynamics. We integrate machine learning potentials with the Boltzmann transport equation (BTE) and molecular dynamics (MD) simulations to conduct a detailed analysis of phonon transport and scattering mechanisms. This computational framework allows for more accurate predictions of thermal conductivity and provides deeper insights into the phonon anharmonicity and glassy thermal transport in crystalline compounds. Our results not only elucidate the origins of the low κ_L in $CuBiSeCl_2$ but also offer a new strategy for further reducing κ_L through the delocalization of atoms and the introduction of softer chemical and vibrational bonds.

II. COMPUTATIONAL METHODS

A. Structural optimization

The Vienna *Ab initio* Simulation Package (VASP) was used to optimize the crystal structure of $CuBiSeCl_2$ [10]. All first-principles calculations are performed by using the projected augmented wave method with Perdew-Burke-Ernzerhof (PBE) exchange-correlation functional [11]. The cut-off energy of 400 eV was used for the wave functions. The van der Waals (vdW) interactions are described by using optB86b functional [12,13]. The force and energy convergence thresholds of 10^{-5} eV/Å and 10^{-10} eV, respectively, were used for both structural relaxation and self-consistent density functional theory (DFT) calculations. The cell and the atoms were fully relaxed in the structural optimization process with the Γ-centered k-point grids of $5 \times 10 \times 3$.

The crystal structure of $CuBiSeCl_2$ belongs to space group *Pnma* with number of 62 and the optimized lattice constants, using PBE potentials, are $a = 8.73$ Å, $b = 4.05$ Å, and $c = 12.99$ Å, in which the vdW interactions are described by the optB86b functional [12,13]. These values are consistent with the experimental values, which are $a = 8.78$ Å, $b = 4.00$ Å, and $c = 13.14$ Å [4]. As illustrated in Fig. 1(b), the phonon spectrum of the PBE functional is free of imaginary frequencies, indicating the dynamical stability of $CuBiSeCl_2$.

*Contact author: zhibin.gao@xjtu.edu.cn

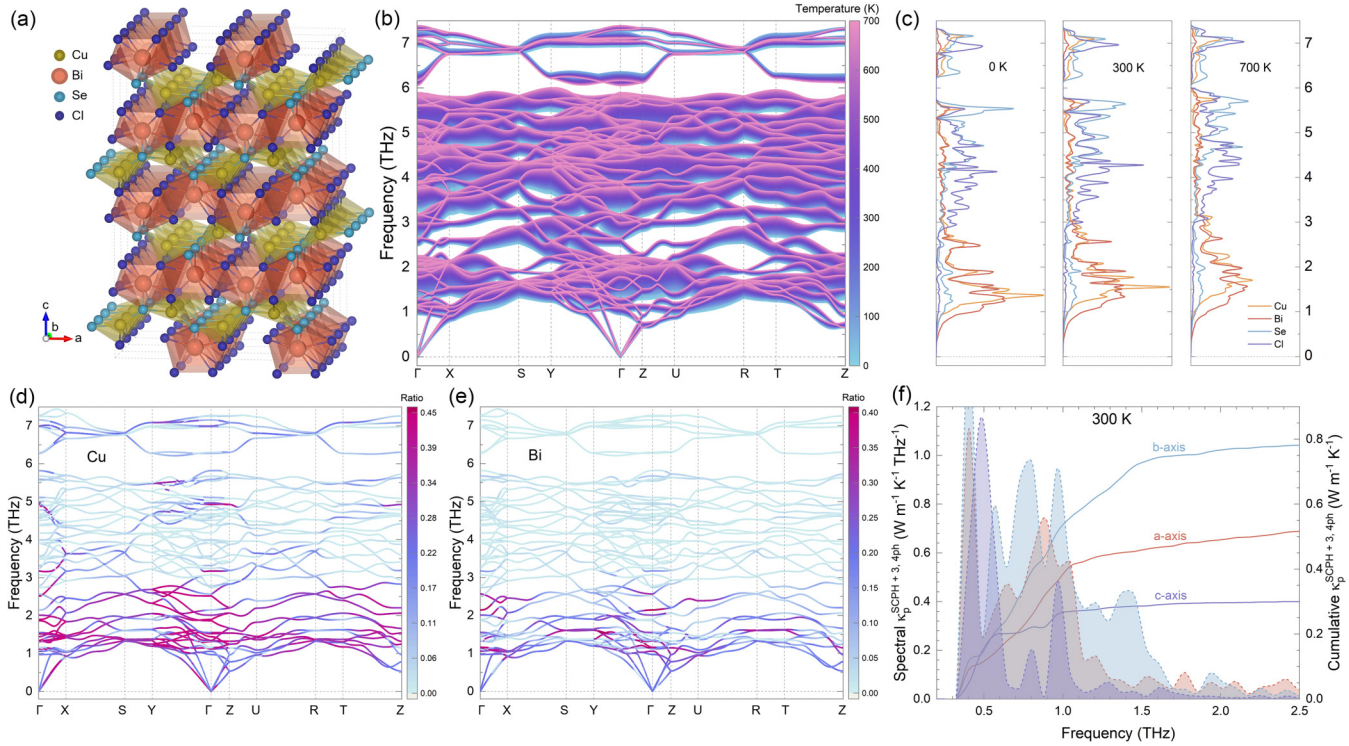

FIG. 1. (a) The conventional cell structure of $CuBiSeCl_2$. The yellow, red, blue, and purple atoms represent Cu, Bi, Se, and Cl, respectively. (b) The temperature-dependent phonon spectrum from T = 0 K to 700 K for $CuBiSeCl_2$, along the high-symmetry points which are defined as Γ (0, 0, 0), X (0.5, 0, 0), S (0.5, 0.5, 0), Y (0, 0.5, 0), Z (0, 0, 0.5), U (0.5, 0, 0.5), R (0.5, 0.5, 0.5), and T (0, 0.5, 0.5). (c) Projected phonon density of states (PDOS) of $CuBiSeCl_2$ at 0 K, 300 K, and 700 K. The atomic participation ratio (APR) of Cu (d) and Bi (e) atoms projected onto the phonon bands at T = 0 K. The color bar represents the atomic participation ratio (APR) for the specified atom in the phonon modes. An APR of 1 (red) indicates that the atom is highly involved in the corresponding vibrational mode, whereas an APR of 0 (blue) signifies little participation of the atom in that mode. (f) Calculated spectral and cumulative particlelike lattice thermal conductivity (κ_p) of $CuBiSeCl_2$ using the SCPH + 3,4ph model at 300 K in different axes.

The primitive cell comprises 20 atoms: four Bi, four Se, four Cu, and eight Cl, respectively.

B. Data generation

The data set was generated using random perturbations with the DPDATA package [14,15]. The deformation ratio of the unit cell was set to 4%, with perturbations in the diagonal part uniformly distributed within the range [−4%, 4%], and perturbations in the off-diagonal part uniformly distributed within the range [−2%, 2%]. The maximum atomic displacement radius was set to 0.4 Å, meaning that the atomic positions were randomly and uniformly distributed within a spherical space of radius 0.4 Å. A total of 600 structures were generated, of which 1/12 were randomly selected as the validation set, while the remaining were used as the training set. The structures of $CuBiSeCl_2$ in the data set were expanded by a $2 \times 4 \times 2$ supercell which contains 320 atoms, and the k-point sampling was set to $1 \times 1 \times 1$. The vdW interactions is also included.

C. Training machine learning potential

To describe the interatomic interaction, machine learning neuroevolution potentials (NEP) was trained on the data set generated by the DFT calculation [16,17].

The NEP parameters can be fitted by minimizing the function [16],

$$
\begin{aligned}
L(z) = {} & \lambda_e \left(\frac{1}{N_{\mathrm{str}}} \sum_{n=1}^{N_{\mathrm{str}}} \left(U^{\mathrm{NEP}}(n,z) - U^{\mathrm{tar}}(n) \right)^2 \right)^{1/2} \\
& + \lambda_f \left(\frac{1}{3N} \sum_{i=1}^{N} \left(F_i^{\mathrm{NEP}}(z) - F_i^{\mathrm{tar}} \right)^2 \right)^{1/2} \\
& + \lambda_v \left(\frac{1}{6N_{\mathrm{str}}} \sum_{n=1}^{N_{\mathrm{str}}} \sum_{\mu\nu} \left(W_{\mu\nu}^{\mathrm{NEP}}(n,z) - W_{\mu\nu}^{\mathrm{tar}}(n) \right)^2 \right)^{1/2} \\
& + \lambda_1 \frac{1}{N_{\mathrm{par}}} \sum_{n=1}^{N_{\mathrm{par}}} |z_n| + \lambda_2 \left(\frac{1}{N_{\mathrm{par}}} \sum_{n=1}^{N_{\mathrm{par}}} z_n^2 \right)^{1/2}, \qquad (1)
\end{aligned}
$$

where N_{str} is the number of structures in the training data set and N is the total number of atoms in all these structures. The first three terms are the weighted averages of the energy, forces, and virial tensor using NEP compared with the DFT results. That is, the loss functions for energy, force, and virial are defined as their root mean square errors between the current NEP predictions and the target values. The last two terms represent ℓ_1 and ℓ_2 regularization. The weights λ_e, λ_f, λ_v, λ_1,

and λ_2 are tunable hyperparameters. When calculating the loss function, we use the following units: eV/atom for energy and virial, and eV/Å for force components.

Since the cutoff values for cubic and quartic interactions used in the phonon thermal conductivity calculations are 4.12 and 3.30 Å, both smaller than the NEP fitting radial cutoff radius 7.0 Å and angular cutoff radius 7.0 Å, indicating the NEP fitting cutoff radius is sufficiently large for the thermal conductivity calculation.

Furthermore, we set the number of basis functions that are used to build the radial and angular descriptor to 14, which is greater than the default value of 8, ensuring sufficient accuracy.

D. Phonon scattering properties

Three-phonon scattering rates can be expressed as

$$\Gamma^{+}_{\lambda\lambda'\lambda''} = \frac{\hbar\pi}{4}\frac{f'_0 - f''_0}{\omega_\lambda\omega_{\lambda'}\omega_{\lambda''}}|V^{+}_{\lambda\lambda'\lambda''}|^2 \delta(\omega_\lambda + \omega_{\lambda'} - \omega_{\lambda''}), \tag{2}$$

$$\Gamma^{-}_{\lambda\lambda'\lambda''} = \frac{\hbar\pi}{4}\frac{f'_0 + f''_0 + 1}{\omega_\lambda\omega_{\lambda'}\omega_{\lambda''}}|V^{-}_{\lambda\lambda'\lambda''}|^2 \delta(\omega_\lambda - \omega_{\lambda'} - \omega_{\lambda''}), \tag{3}$$

where, for simplicity, f'_0 stands for $f_0(\omega_{\lambda'})$ and f''_0 denotes $f_0(\omega_{\lambda''})$. The term $\Gamma^{+}_{\lambda\lambda',\lambda''}$ corresponds to an absorption process, where two incident phonons $(\omega_\lambda, \omega_{\lambda'})$ merge into a single phonon whose frequency is their sum. Meanwhile, $\Gamma^{-}_{\lambda\lambda',\lambda''}$ describes an emission process, in which one phonon splits into two $(\omega_{\lambda'}, \omega_{\lambda''})$ [18].

Phonon density of states (DOS) is calculated with a linear tetrahedron method which is default in PHONOPY [19]. Projected DOS is calculated using "PDOS = AUTO". Without specifying projection direction, PDOS is computed as sum of $g^j(\omega, \hat{\mathbf{n}})$ projected onto Cartesian axes x, y, z,

$$g^j(\omega) = \sum_{\hat{\mathbf{n}}=\{x,y,z\}} g^j(\omega, \hat{\mathbf{n}}), \tag{4}$$

where j is the atom indices and $\hat{\mathbf{n}}$ is the unit projection direction vector.

Mean-square displacement of different atoms is also calculated using PHONOPY package [19]. The expectation value of the squared atomic displacement is calculated as

$$\langle|u^\alpha(jl,t)|^2\rangle = \frac{\hbar}{2Nm_j}\sum_{\mathbf{q},\nu}\omega_\nu(\mathbf{q})^{-1}(1+2n_\nu(\mathbf{q},T))\left|e^\alpha_\nu(j,\mathbf{q})\right|^2, \tag{5}$$

where $n_\nu(\mathbf{q}, T)$ is the phonon population, which is given by

$$n_\nu(\mathbf{q},T) = \frac{1}{\exp(\hbar\omega_\nu(\mathbf{q})/k_\mathrm{B}T) - 1}, \tag{6}$$

T is the temperature, and k_B is the Boltzmann constant.

Atomic participation ratio (APR) is calculated with the ALAMODE package and is defined as follows:

$$\mathrm{APR}_{\mathbf{q}j,\kappa} = \frac{|\mathbf{e}(\kappa;\mathbf{q}j)|^2}{M_\kappa}\Bigg/\left(N_\kappa\sum_{\kappa}^{N_\kappa}\frac{|\mathbf{e}(\kappa;\mathbf{q}j)|^4}{M_\kappa^2}\right)^{1/2}. \tag{7}$$

APR is an atomic decomposition of PR that satisfies $\mathrm{PR}_{\mathbf{q}j} = \sum_\kappa(\mathrm{APR}_{\mathbf{q}j,\kappa})^2$.

E. Lattice thermal conductivity

The lattice thermal conductivity κ_p based on Peierls-Boltzmann transport theory is given by [20],

$$\kappa_p = \frac{\hbar^2}{k_B T^2 V N_0}\sum_\lambda n_\lambda(n_\lambda+1)\omega_\lambda^2 \boldsymbol{v}\lambda\otimes\boldsymbol{v}\lambda\boldsymbol{\tau}_\lambda, \tag{8}$$

where $\hbar$ denotes the reduced Planck constant, k_B is the Boltzmann constant, T is the absolute temperature, V is the volume of the primitive unit cell, and N_0 is the number of phonon wave vectors sampled in the first Brillouin zone. The variables n_λ, ω_λ, $\boldsymbol{v}_\lambda$, and τ_λ indicate the phonon population, frequency, group velocity, and lifetime for the λ mode which is defined by wave vector q and branch index s.

In the interatomic force constants (IFCs) calculations, a $2\times4\times1$ supercell of $CuBiSeCl_2$ was used. Third- and fourth-order IFCs were calculated up to the eighth- and third-nearest neighbors, respectively [21,22]. The q-mesh grid was set to $6\times12\times4$ for four-phonon (4ph) processes and $10\times20\times7$ for three-phonon (3ph) processes. The self-consistent phonon (SCPH) approximation [23,24] was applied to incorporate first-order phonon frequency corrections due to quartic anharmonicity, which enhances accuracy for materials with soft phonon modes and significant anharmonicity. The SCPH is described by

$$\Omega_\lambda^2 = \omega_\lambda^2 + 2\Omega_\lambda\sum_{\lambda_1} I_{\lambda\lambda_1}, \tag{9}$$

where ω_λ represents the initial phonon frequency derived from the harmonic approximation, and Ω_λ denotes the temperature-dependent renormalized phonon frequency. The scalar $I_{\lambda\lambda_1}$ is calculated as follows:

$$I_{\lambda\lambda_1} = \frac{\hbar}{8N_0}\frac{V^{(4)}(\lambda,-\lambda,\lambda_1,-\lambda_1)}{\Omega_\lambda\Omega_{\lambda_1}}[1+2n_\lambda(\Omega_{\lambda_1})], \tag{10}$$

where $V^{(4)}$ represents the fourth-order IFCs in the reciprocal space, and the phonon population n_λ follows the Bose-Einstein distribution. Equations (9) and (10) both possess the parameters $I_{\lambda\lambda_1}$ and Ω_λ, allowing the SCPH equation to be solved iteratively. Also, we fix the volume in self-consistent phonon calculation which means that thermal expansion was not considered in temperature-dependent renormalized phonon frequency [25].

To enhance the accuracy of the lattice thermal conductivity, the coherent phonon κ_c describing tunneling of coherent phonons, was also included and is defined as [26]

$$\kappa_c = \frac{\hbar^2}{k_B T^2 V N_0}\sum_{\boldsymbol{q}}\sum_{s\neq s'}\frac{\omega_{\boldsymbol{q}}^s+\omega_{\boldsymbol{q}}^{s'}}{2}\boldsymbol{v}_{\boldsymbol{q}}^{s,s'}\boldsymbol{v}_{\boldsymbol{q}}^{s',s} \times\frac{\omega_{\boldsymbol{q}}^s n_{\boldsymbol{q}}^s\left(n_{\boldsymbol{q}}^s+1\right)+\omega_{\boldsymbol{q}}^{s'}n_{\boldsymbol{q}}^{s'}\left(n_{\boldsymbol{q}}^{s'}+1\right)}{4\left(\omega_{\boldsymbol{q}}^{s'}-\omega_{\boldsymbol{q}}^s\right)^2+\left(\Gamma_{\boldsymbol{q}}^s+\Gamma_{\boldsymbol{q}}^{s'}\right)^2} \times\left(\Gamma_{\boldsymbol{q}}^s+\Gamma_{\boldsymbol{q}}^{s'}\right), \tag{11}$$

where $\hbar$ is the reduced Planck constant, k_B is Boltzmann constant, V is the primitive cell volume, and N_0 is the total number of sampled phonon vectors.

Additionally, the temperature-dependent κ_L of $CuBiSeCl_2$ is also calculated from homogeneous nonequilibrium molecular dynamics (HNEMD) simulations [27–29], an average result of 2 ns for five times with the model cell around 75 Åalong each edge. The total heat flow in the system is the sum of contributions from each atom

$$J = \sum_i \sum_{j \neq i} \mathbf{r}_{ij} \left(\frac{\partial U_j}{\partial \mathbf{r}_{ji}} \cdot \mathbf{v}_i \right), \tag{12}$$

where J in the Green-Kubo method for calculating thermal conductivity, with r_{ij} is the distance vector between atoms i and j, U is the potential energy, and v is velocity. In the HNEMD method, each atom in the system is subjected to an external force to drive it out of equilibrium. This force, expressed as

$$\vec{F}_{\text{ext},i} = E_i \vec{F}_e + \vec{F}_e \cdot \vec{W}_i, \tag{13}$$

This approach offers a way to compute thermal conductivity. Unlike the NEMD method, the HNEMD framework maintains the system in a uniform nonequilibrium state, without explicit heat sources or sinks. As a result, phonon boundary scattering is absent, and heat circulates due to periodic boundary conditions along the transport direction. This method produces finite-size effects similar to those seen in the EMD approach.

III. RESULTS AND DISCUSSION

A. Anharmonic lattice dynamics

The impact of fourth-order anharmonicity on the phonon spectra at finite temperatures is depicted in Fig. 1(b), using the IFCs obtained from Machine Learning Potential. The overall phonon hardening is observed in crystalline $CuBiSeCl_2$ as the temperature increases from 0 to 700 K. This suggests the presence of strong lattice anharmonicity in $CuBiSeCl_2$ and highlights the importance of properly treating temperature renormalization [23,30–33]. In particular, the low-frequency phonons below 3 Thz are predominantly influenced by the Cu (yellow) and Bi (red) atoms, as evidenced by the projected PDOS in Fig. 1(c).

Furthermore, atom-decomposed partial DOS in Fig. 1(c) and atomic participation ratios in Figs. 1(d)–1(e) show that Cu and Bi atoms contribute mostly to the low-lying flattened phonon bands in the frequency lower than 2.0 THz.

In contrast, the high-frequency phonon modes around 6 THz in $CuBiSeCl_2$ are predominantly contributed by Se and Cl atoms and exhibit a temperature-dependent softening in Fig. 1(c). Cumulated κ_p shown in Fig. 1(f) also approve that low frequency phonons less than 1.5 THz are the main contributor to the κ_p of $CuBiSeCl_2$. These indicate that the phonon vibrations of Cu and Bi atoms predominantly govern κ_p in $CuBiSeCl_2$ [34–36].

B. Delocalization of copper atoms

Figure 2(a) shows the mean-square displacements (MSDs) of atoms obtained by both harmonic approximation (HA) and self-consistent phonon (SCPH) in $CuBiSeCl_2$ as a function of temperature calculations along the b axis. MSD is a measure of the deviation of the position of an atom with respect to a reference position over time. It indicates the atomic displacements of Cu are significantly larger than those of other atoms Bi, Se, and Cl, suggesting that the bonding of Cu atoms is heavily delocalized and soft [30].

Meanwhile, the MSDs calculated by HA typically exhibit overestimation, while anharmonic effects suppress the vibrational amplitudes of all atoms [30]. The discrepancy between them can intuitively quantify the role of anharmonic effects. Figure 2(b) illustrates the differences in MSDs between the HA and SCPH calculations along all three axes for $CuBiSeCl_2$. It can be observed that the MSDs differences of Cu atoms are larger than those of other elements in all three directions. Particularly, the MSDs difference along b axis is the largest, indicating strong phonon anharmonicity in this direction. Besides, the U-shaped potential energy of Cu atom displacement can be well fitted by a fourth-order polynomial in Fig. S8 [37], also qualitatively indicating strong high-order phonon anharmonicity [38].

The red color corresponds to complete localization and blue corresponds to complete delocalization of electrons in two-dimensional (2D) electron localization function (ELF) of $CuBiSeCl_2$ shown in Fig. 2(c). The deeper blue color between Cu and Cl or Se atoms indicates there is no significant electron wave function overlap between Cu and its surrounding atoms, further suggesting that no strong bonding is formed and a greater degree of delocalization for Cu atoms.

The κ_L of $CuBiSeCl_2$ at 300 K in Figs. 2(d)–2(f), calculated using HNEMD is the averaged result from five 2 ns simulation runs, totally 10 ns [27–29]. We employed precise NEP to obtain the intrinsic κ_L of $CuBiSeCl_2$, highlighted in red color in Figs. 2(d)–2(f). The thicker solid line corresponds to the averaged result, and the converged κ_L values are marked on the right side of the figure. These values indicate a significantly lower intrinsic κ_L along the c axis (0.34 W m^{-1} K^{-1}) compared to the a and b axes (0.50 and 0.55 W m^{-1} K^{-1}), consistent with the final result shown in Fig. 4(d) [31,39].

Based on Figs. 2(a)–2(c), we observe a significant difference in the delocalization of Cu compared to Bi, Se, and Cl. To investigate the impact of the delocalization of different atoms on κ_L, we used the same HNEMD method to calculate κ_L along a, b, and c axes of the system after fixing different types of atoms by setting the velocities and forces acting on the selected atoms to zero with the function implanted in GPUMD software package [16]. The results are shown in Figs. 2(d)–2(f). Yellow, purple, and blue represent the fixed atoms of Cu, Bi, and Se, respectively. In all three directions, for the cases where Bi and Se atoms are fixed, a significant decrease in κ_L compared to the intrinsic values is observed, indicating that the strong localization of Bi and Se atoms enhances the phonon transport of $CuBiSeCl_2$. However, fixing Cu in the a and b axes reveals its counterintuitive phenomenon, as its fixation leads to an increase in κ_L compared to the intrinsic value by 0.08 and 0.67 W m^{-1} K^{-1}, respectively. This highlights that the delocalization of Cu has a negative impact on κ_L, especially on the b axis [40].

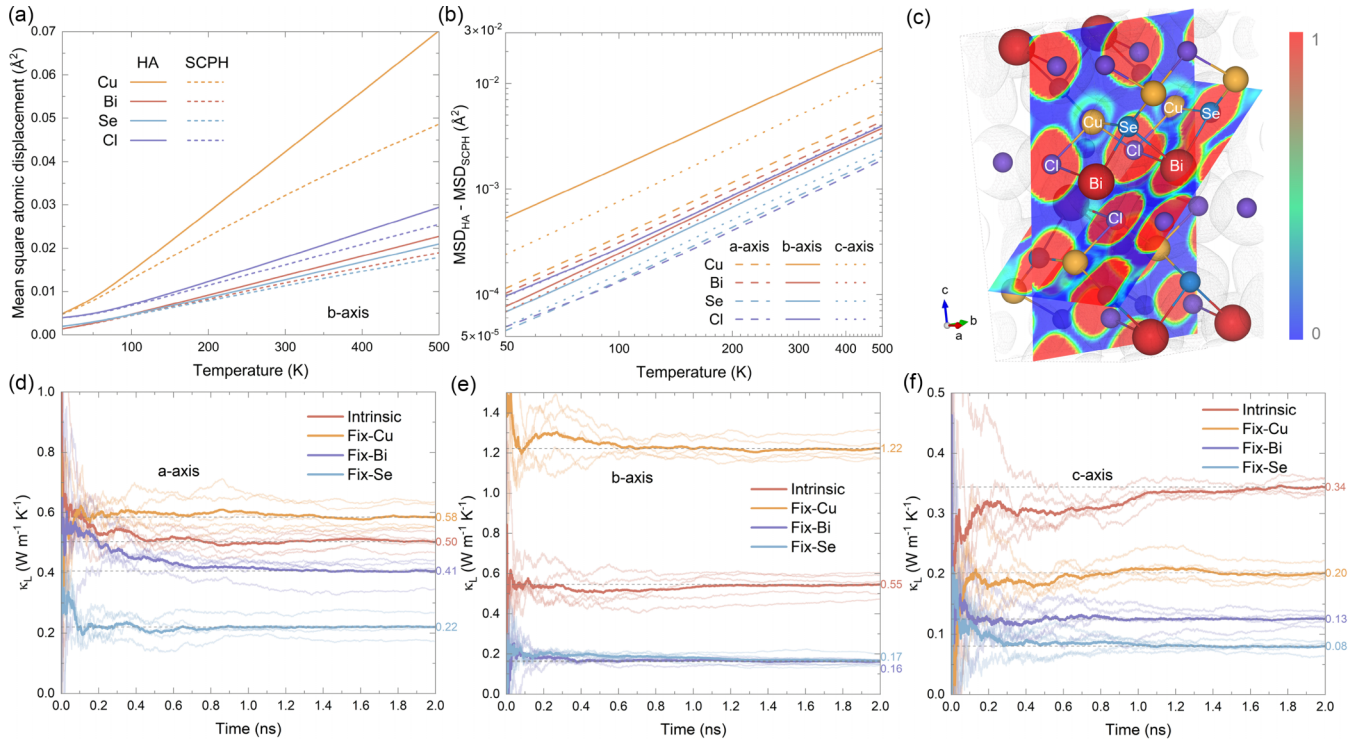

FIG. 2. (a) The mean square atomic displacements (MSDs) with temperatures for $CuBiSeCl_2$. The solid and dashed lines correspond to the MSDs obtained by harmonic approximation (HA) and self-consistent phonon (SCPH) calculations, respectively. (b) Difference between MSDs obtained by HA and SCPH approaches in a axis, b axis, and c axis. (c) Electron localization function (ELF) of $CuBiSeCl_2$. The red color corresponds to complete localization and the blue color corresponds to complete delocalization of electrons. κ_L predicted by the HNEMD method with NEP vs integration time for $CuBiSeCl_2$ in a axis (d), b axis (e), and c axis (f), respectively. The values labeled on the right represent the averaged final converged κ_L.

C. Thermal transport properties

From Eqs. (8) and (11), κ_L is a result of coupling between the harmonic and the anharmonic terms. To further elucidate the microscopic origins of ultralow κ_L, we analyzed several critical parameters influencing κ_L, such as heat capacity, phonon velocities, scattering rates, Grüneisen parameter, weighted scattering phase space, and lifetimes of $CuBiSeCl_2$, as shown in Fig. 3.

Heat capacity (C_V) is $3Nk_B$ in a typical solid at high temperature (the Dulong-Petit limit), where N is the number of particles and k_B is the Boltzmann constant. Here in Fig. 3(a), with temperature going higher than 300 K, the C_V given out by DFT calculation is very close to the theoretical value $3Nk_B = 0.295$ J g^{-1} K^{-1}. Also, this value of $CuBiSeCl_2$ is even lower than 0.36 J g^{-1} K^{-1} of liquidlike thermoelectric Cu_2Se [41] and a little higher than 0.156 J g^{-1} K^{-1} of renowned PbTe [42].

Since κ_L is proportional to the square of the phonon group velocity (v^2), we computed the frequency-dependent v^2 values at 300 K, presented in Fig. 3(b). The maximum v^2 of $CuBiSeCl_2$ reaches only 20 km^2 s^{-2}, which is slightly higher in all directions than that of PbTe (approximately 14 km^2 s^{-2} at 300 K with $\kappa_L = 2$ W m^{-1} K^{-1}) [43]. For comparison, group velocities of modular inorganic $Bi_4O_4SeCl_2$ with bonding anisotropy and mismatch [44] exhibits the same order, with a maximum of around 8 km^1 s^{-1}, aligning with its exceptionally low κ_L of 0.1 W m^{-1} K^{-1} at 300 K [45]. This underscores that the limited κ_L in $CuBiSeCl_2$ is also a result of its reduced v. Additionally, at 300 K, the low-frequency phonon spectrum shifts rightward compared to the HA, while the high-frequency shifts leftward, indicating phonon hardening in the low-frequency range and softening in the high-frequency range, as also illustrated in Fig. 1(b).

The extent of anharmonicity is typically measured by the Grüneisen parameter, illustrated in Fig. 3(c). Below 1.5 THz, there is an intertwinement between the acoustic and optical phonon branches at 300 K. This is closely linked to the Cu and Bi atoms and the bonding hierarchy. Moreover, the total Grüneisen value is 1.50, close to PbTe value of 1.45 [46], indicating $CuBiSeCl_2$ exhibits substantial anharmonicity.

To deepen the analysis of phonon scattering processes, we computed the phonon scattering phase space, which evaluates the channel available for phonon-phonon scattering. As shown in Fig. 3(d), the weighted phase space for both three-phonon (3ph) and four-phonon (4ph) processes rises with temperature, from 300 to 700 K. Notably, the 4ph phase space exceeds that of 3ph processes, leading to a significant contribution of 4ph scattering in $CuBiSeCl_2$. The peak in the 4ph phase space around 1.5 THz aligns with the PDOS for Cu atoms, shown in Fig. 1(c). The presence of low-energy flattening modes enhances 4ph scattering channels, which elevates the 4ph scattering rates and, consequently, further limits thermal transport in $CuBiSeCl_2$.

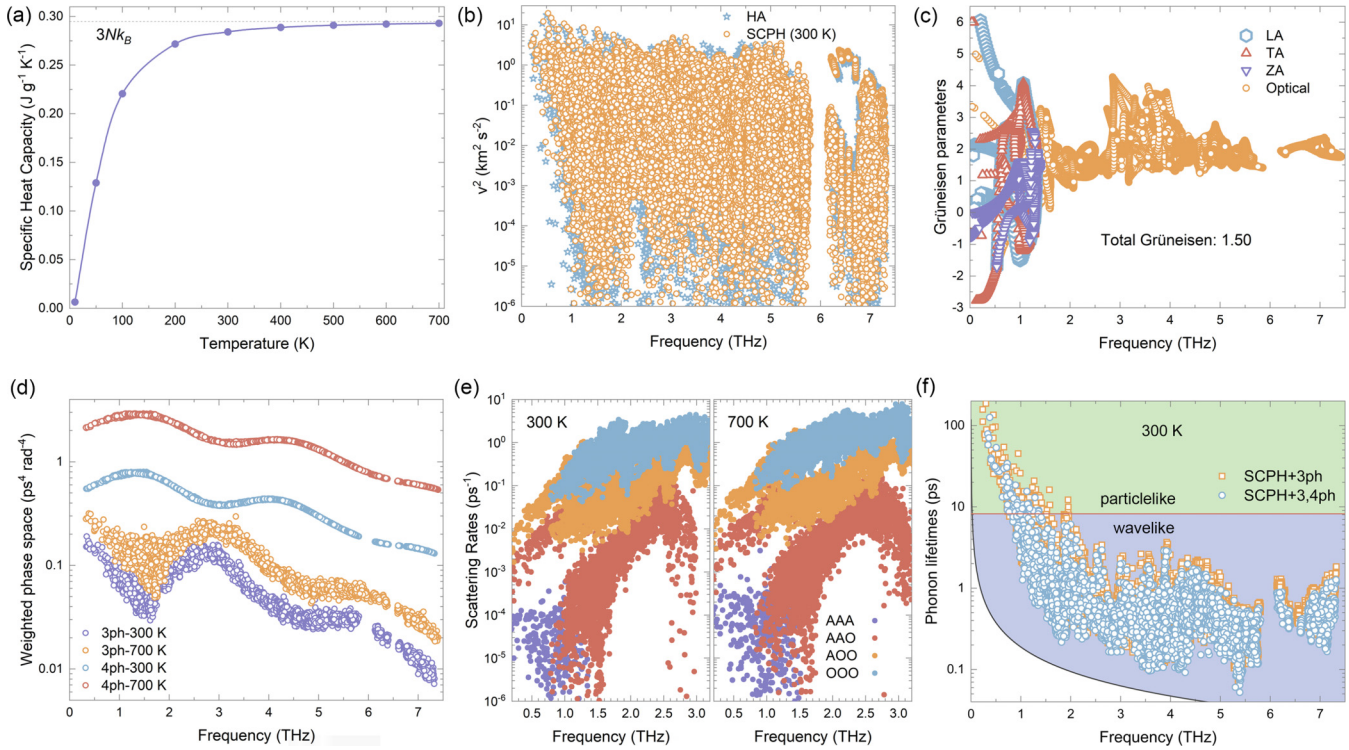

FIG. 3. Microscopy heat transport parameters of $CuBiSeCl_2$. (a) Specific heat capacity at constant volume (C_V). (b) Squared phonon group velocities (v^2) in the harmonic approximation and anharmonic renormalization approximation at 300 K. (c) Grüneisen parameter. (d) Weighted phonon scattering phase space of 3ph and 4ph at 300 K and 700 K. (e) Phonon scattering rates of 3ph at 300 K and 700 K. (f) Phonon lifetime of at 300 K. The red horizontal line represents the Wigner limit, expressed as $\tau_{\text{threshold}} = [\Delta\omega_{\text{avg}}]^{-1}$, where $\Delta\omega_{\text{avg}}$ is the average phonon interband spacing [47]. $\Delta\omega_{\text{avg}}$ is determined by $\omega_{\max}/3N_{\text{at}}$, with N_{at} being the number of atoms per unit cell and $\omega_{\max}$ being the highest frequency. Phonons with lifetimes longer than $\tau_{\text{threshold}}$ primarily affect thermal conductivity via population mechanisms (green region), while shorter lifetimes contribute to wavelike tunneling (blue region). The black curve shows the Ioffe-Regel limit, $\tau_{\text{IR}} = 2\pi/\omega$, in which ω is the phonon frequency. Phonons lifetime exceeding τ_{IR} can be described by the Wigner transport equation [33,39,48].

We evaluate the 3ph scattering channels involving three acoustic phonons (AAA, purple), two acoustic phonons combining with one optical phonon (AAO, red), and one acoustic phonon combining with two optical phonons (AOO, orange), as shown in Fig. 3(e). The scattering process of the AAO mode is found to be as strong as the AOO mode below 1 THz, meaning that the AAO and AOO phonons play important roles in reduce heat transport. Also, as temperature increases to 700 K in Fig. 3(e) the scattering process of AAA mode becomes much stronger compared to other modes, the maximum scattering rates are changed from around 10^{-4} to 10^{-3} ps^{-1}, which significantly reduce the κ_L of $CuBiSeCl_2$ at higher temperatures.

Recently, a seminal concept is introduced known as the Wigner limit in time, which has been applied to distinguish phonons into various thermal transport regimes, primarily consisting of particlelike propagation and wavelike tunneling [26,47,49]. The Wigner limit in time is characterized as $\tau_{\text{threshold}} = 3N_{\text{at}}/\omega_{\max}$, where N_{at} represents the number of atoms in the unit cell, and $\omega_{\max}$ denotes the maximum phonon frequency. According to this criterion, phonons with lifetimes exceeding $\tau_{\text{threshold}}$ exhibit particlelike behavior and are the main contributors to the κ_p from phonon population. In contrast, those with shorter lifetime exhibit wavelike tunneling behavior, primarily contributing to the κ_c from coherence phonons.

For the case of $CuBiSeCl_2$, after accounting for both 3ph and 4ph scattering mechanisms, most phonons have lifetimes below the Wigner limit at 300 K, underscoring the significance of wavelike tunneling as a transport channel, as illustrated in Fig. 3(f). This suggests that the coherence contribution from wavelike tunneling plays an important role in the overall thermal conductivity of $CuBiSeCl_2$, as observed in Fig. 4.

Notably, when 4ph scattering is incorporated into SCPH + 3, 4ph model, the particlelike propagation channel is notably suppressed compared with SCPH + 3ph model, making the wavelike tunneling channel more important in thermal transport. The findings illustrate the limitations of traditional phonon-gas models in explaining the thermal behavior of $CuBiSeCl_2$ and emphasize the need for advanced methods, such as the SCPH + 3, 4ph together with κ_c, to more accurately capture the underlying heat transfer mechanisms in this material.

We further calculated the temperature-dependent κ_L across four theoretical models to examine the effects of phonon energy renormalization and multiphonon interactions arising from cubic and quartic phonon anharmonicities, as shown in Fig. 4(a). Results reveal that κ_L exhibits anisotropy in Fig. 4(b), with the κ_p along the a and b axes being approximately 100% and 160% higher, respectively, than along the c axis. The lowest level of thermal transport theory, HA + 3ph

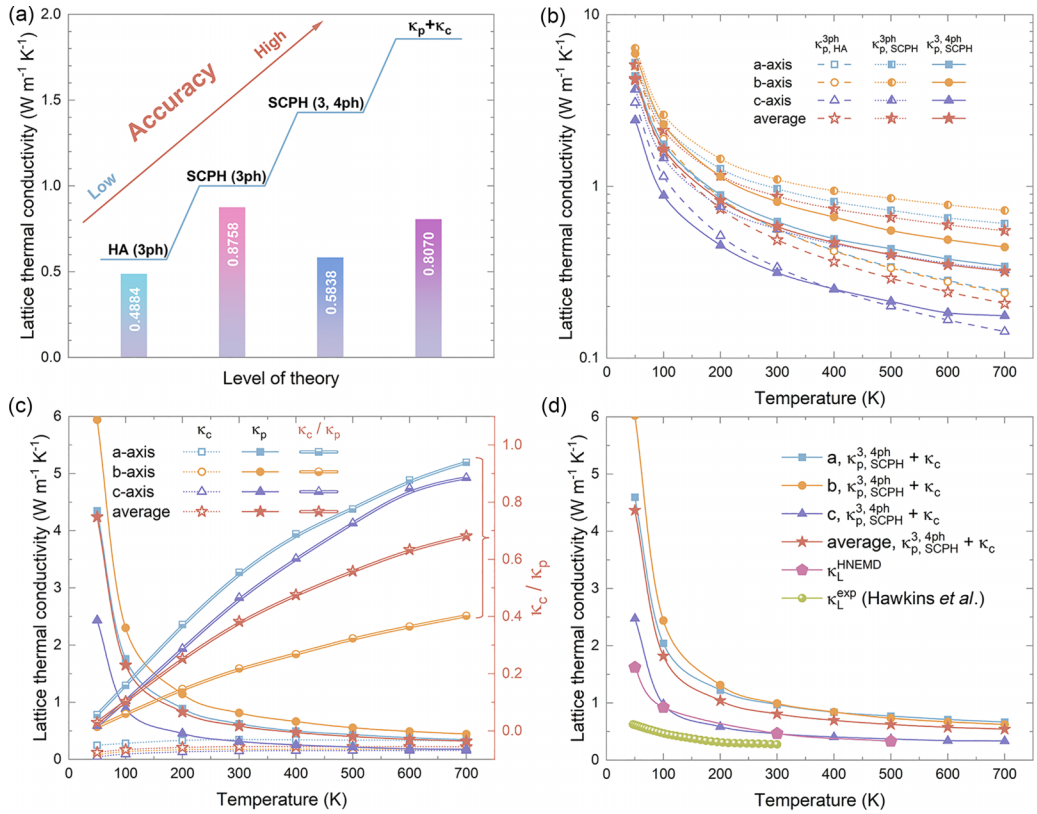

FIG. 4. (a) A schematic illustration demonstrating the prediction accuracy of κ_L across different hierarchical thermal transport methods, including the HA + 3ph, SCPH + 3ph, SCPH + 3, 4ph, and SCPH + 3, 4ph + κ_c, where 3ph indicates only three-phonon scattering is included and 3,4ph means both three-phonon and four-phonon scattering are considered. HA means harmonic approximation, and SCPH is short for self-consistent phonon. (b) κ_p of $CuBiSeCl_2$ using HA + 3ph, SCPH + 3ph, SCPH + 3, 4ph approaches. (c) κ_p of $CuBiSeCl_2$ compare with κ_c. (d) κ_L of $CuBiSeCl_2$ using the BTE method and MD method compare with experimental values [4].

model gives $\kappa_{p,\mathrm{HA}}^{3\mathrm{ph}}$ values in the c-axis direction of 3.08, 0.34, and 0.14 W m^{-1} K^{-1} at 50, 300, and 700 K, respectively.

As previously noted, anharmonic phonon renormalization plays a critical role in predicting finite-temperature κ_L in complex compounds. By including phonon energy shifts in Fig. 4(b), we extend the HA+3ph model to the more precise SCPH + 3ph model, yielding $\kappa_{p,\mathrm{SCPH}}^{3\mathrm{ph}}$ values of 3.67, 0.56, and 0.33 W m^{-1} K^{-1} in the c axis at 50, 300, and 700 K, respectively, 19%, 67%, and 129% higher than $\kappa_{p,\mathrm{HA}}^{3\mathrm{ph}}$, indicating significant anharmonic phonon renormalization in $CuBiSeCl_2$ that intensifies with temperature. This trend aligns with Fig. 1(b), which shows pronounced phonon frequency shifts as temperature increases.

Moreover, quartic anharmonicity not only induces substantial phonon frequency shifts but also results in pronounced 4ph scattering. We obtained the average $\kappa_{p,\mathrm{SCPH}}^{3,4\mathrm{ph}}$ values of 4.24, 0.58, and 0.32 W m^{-1} K^{-1} at 50, 300, and 700 K, respectively, shown in Fig. 4(b). These values represent reductions of 17%, 33%, and 42% compared to $\kappa_{p,\mathrm{SCPH}}^{3\mathrm{ph}}$, highlighting the impact of 4ph scattering [31,36,50]. This result confirms that phonon hardening and 4ph scattering, driven by quartic anharmonicity, have counteractive effects on κ_L.

Nevertheless, the coherence contributions are not negligible as shown in Fig. 4(c). By further considering the off-diagonal terms of heat flux operators, the total κ_L significantly enhanced by incorporating both $\kappa_{p,\mathrm{SCPH}}^{3,4\mathrm{ph}}$ and κ_c [26]. The ratio κ_c/κ_p (red star) is greater than 0.5 at 500 K and exhibits a pronounced increase with temperature. Specifically, in the a-axis direction, the ratio of κ_c/κ_p (blue square) reaches 0.94 at 700 K, which is 1.7 times larger than the 0.55 observed at 300 K. This observation suggests that the contribution of κ_c is equally important as κ_p in crystalline $CuBiSeCl_2$ especially in the a axis and high temperature. The dominant role of coherence contribution in thermal transport was also observed in other complex compounds such as $Cs_2AgBiBr_6$ [48], $Cu_{12}Sb_4S_{13}$ [51], $CsPbBr_3$ [52], $TlAgI_2$ [33], $La_2Zr_2O_7$ [47], Tl_9SbTe_6 [39], and even simple cubic CsCl [50].

We further use the HNEMD method to assess the intrinsic κ_L of $CuBiSeCl_2$ [16,27,29]. Since the MD method includes full-order lattice anharmonicity larger than those lattice anharmonicity considered in BTE up to fourth-order, the results are relatively smaller than those obtained from BTE. Figure 4(d) reveals that the average $\kappa_{p,\mathrm{SCPH}}^{3,4\mathrm{ph}}$ at 300 K is 0.584 W m^{-1} K^{-1}, larger than 0.466 W m^{-1} K^{-1} from HNEMD. The latter HNEMD result is a little larger than the experimental κ_L, which is 0.275 W m^{-1} K^{-1} at 300 K. This could result from their nondense sample, with a density of only 88% [4,37,53,54]. The result suggests that the higher than fourth-

order lattice anharmonicity could be crucial for capturing the ultralow κ_L of complex compounds such as $CuBiSeCl_2$.

IV. CONCLUSION

In summary, this study explores the thermal transport properties of $CuBiSeCl_2$ by utilizing a combination of self-consistent phonon theory based on machine learning potentials [16,17,55], first-principles calculations, and a unified approach of the Wigner transport equation to account for both coherent and population contributions to thermal transport. The neuroevolution potentials achieve a level of accuracy comparable to DFT in predicting energies and atomic forces. The temperature-dependent force constants reveal a significant phonon hardening effect over nearly the entire frequency spectrum, indicating strong lattice anharmonicity in $CuBiSeCl_2$. This leads to ultralow κ_L of 0.81 W m^{-1} K^{-1} at 300 K. By using the HNEMD method, where full-order lattice anharmonicity is considered, the κ_L decreases further to 0.47 W m^{-1} K^{-1}, closely aligning with experimental measurements [4,53].

κ_c/κ_p exceeds 0.5 above 400 K, indicating that the off-diagonal components of heat flux operators play a significant role in the thermal transport of $CuBiSeCl_2$. Most strikingly, we trace ultralow κ_L of $CuBiSeCl_2$ to the delocalization of loosely bound copper atoms. Our work may shed light on further suppressing κ_L and seek for promising thermoelectrics by adjusting bonding strength, localization, and delocalization of electrons [41,56,57].

ACKNOWLEDGMENTS

The authors gratefully acknowledge discussions with J. Zheng. We acknowledge the support from the National Natural Science Foundation of China (No. 52250191), and the Fundamental Research Funds for the Central Universities. This work is sponsored by the Key Research and Development Program of the Ministry of Science and Technology (No. 2023YFB4604100). We also acknowledge the support by HPC Platform, Xi'an Jiaotong University.

DATA AVAILABILITY

The data that support the findings of this article are openly available [37].

[1] H. Kageyama, K. Hayashi, K. Maeda, J. P. Attfield, Z. Hiroi, J. M. Rondinelli, and K. R. Poeppelmeier, Expanding frontiers in materials chemistry and physics with multiple anions, Nat. Commun. **9**, 772 (2018).

[2] X. Shen, K. Pal, P. Acharyya, B. Raveau, P. Boullay, O. I. Lebedev, C. Prestipino, S. Fujii, C.-C. Yang, I.-Y. Tsao, A. Renaud, P. Lemoine, C. Candolfi, and E. Guilmeau, Lone pair induced 1D character and weak cation anion interactions: Two ingredients for low thermal conductivity in mixed-anion metal chalcohalide $CuBiSCl_2$, J. Am. Chem. Soc. **146**, 29072 (2024).

[3] C. Ming *et al.*, Mixed chalcogenide-halides for stable, lead-free and defect-tolerant photovoltaics: Computational screening and experimental validation of $CuBiSCl_2$ with ideal band gap, Adv. Funct. Mater. **32**, 2112682 (2022).

[4] C. J. Hawkins, J. A. Newnham, B. Almoussawi, N. L. Gulay, S. L. Goodwin, M. Zanella, T. D. Manning, L. M. Daniels, M. S. Dyer, T. D. Veal, J. B. Claridge, and M. J. Rosseinsky, Structure, and properties of $CuBiSeCl_2$: A chalcohalide material with low thermal conductivity, Chem. Mater. **36**, 4530 (2024).

[5] X. Chen, Q. Jing, and K. M. Ok, $Pb_{18}O_8Cl_{15}I_5$: A polar lead mixed oxyhalide with unprecedented architecture and excellent infrared nonlinear optical properties, Angew. Chem. Int. Ed. **59**, 20323 (2020).

[6] Y. Tsujimoto, C. I. Sathish, K.-P. Hong, K. Oka, M. Azuma, Y. Guo, Y. Matsushita, K. Yamaura, and E. Takayama-Muromachi, Crystal structural, magnetic, and transport properties of layered cobalt oxyfluorides, $Sr_2CoO_{3+x}F_{1x}$ ($0 < x < 0.15$), Inorg. Chem. **51**, 4802 (2012).

[7] Y. Kamihara, H. Hiramatsu, M. Hirano, R. Kawamura, H. Yanagi, T. Kamiya, and H. Hosono, Iron-based layered superconductor: LaOFeP, J. Am. Chem. Soc. **128**, 10012 (2006).

[8] J. M. Hodges, Y. Xia, C. D. Malliakas, T. J. Slade, C. Wolverton, and M. G. Kanatzidis, Mixed-valent copper chalcogenides: Tuning structures and electronic properties using multiple anions, Chem. Mater. **32**, 10146 (2020).

[9] H. Wu, A. Erbing, M. B. Johansson, J. Wang, C. Kamal, M. Odelius, and E. M. J. Johansson, Mixed-halide double perovskite Cs_2AgBiX_6 (X = Br, I) with tunable optical properties via anion exchange, ChemSusChem **14**, 4507 (2021).

[10] G. Kresse and J. Furthmüller, Efficient iterative schemes for *ab initio* total-energy calculations using a plane-wave basis set, Phys. Rev. B **54**, 11169 (1996).

[11] J. P. Perdew, K. Burke, and M. Ernzerhof, Generalized gradient approximation made simple, Phys. Rev. Lett. **77**, 3865 (1996).

[12] J. Klimeš, D. R. Bowler, and A. Michaelides, Chemical accuracy for the van der Waals density functional, J. Phys.: Condens. Matter **22**, 022201 (2010).

[13] J. C. V. Klimeš, D. R. Bowler, and Michaelides, Van der, Waals density functionals applied to solids, Phys. Rev. B **83**, 195131 (2011).

[14] L. Zhang, J. Han, H. Wang, R. Car, and W. Weinan, Deep potential molecular dynamics: A scalable model with the accuracy of quantum mechanics, Phys. Rev. Lett. **120**, 143001 (2018).

[15] H. Wang, L. Zhang, J. Han, and E. Weinan, DeePMD-kit: A deep learning package for many-body potential energy representation and molecular dynamics, Comput. Phys. Commun. **228**, 178 (2018).

[16] Z. Fan *et al.*, GPUMD: A package for constructing accurate machine-learned potentials and performing highly efficient atomistic simulations, J. Chem. Phys. **157**, 114801 (2022).

[17] H. Dong, Y. Shi, P. Ying, K. Xu, T. Liang, Y. Wang, Z. Zeng, X. Wu, W. Zhou, S. Xiong, S. Chen, and Z. Fan, Molecular dynamics simulations of heat transport using machine-learned potentials: A mini-review and tutorial on GPUMD

with neuroevolution potentials, J. Appl. Phys. **135**, 161101 (2024).
[18] W. Li, J. Carrete, N. A. Katcho, and N. Mingo, ShengBTE: A solver of the Boltzmann transport equation for phonons, Comput. Phys. Commun. **185**, 1747 (2014).
[19] A. Togo and I. Tanaka, First principles phonon calculations in materials science, Scr. Mater. **108**, 1 (2015).
[20] T. Feng and X. Ruan, Quantum mechanical prediction of four-phonon scattering rates and reduced thermal conductivity of solids, Phys. Rev. B **93**, 045202 (2016).
[21] Z. Han, X. Yang, W. Li, T. Feng, and X. Ruan, FourPhonon: An extension module to ShengBTE for computing four-phonon scattering rates and thermal conductivity, Comput. Phys. Commun. **270**, 108179 (2022).
[22] Y. Ouyang, C. Yu, J. He, P. Jiang, W. Ren, and J. Chen, Accurate description of high-order phonon anharmonicity and lattice thermal conductivity from molecular dynamics simulations with machine learning potential, Phys. Rev. B **105**, 115202 (2022).
[23] T. Tadano and S. Tsuneyuki, Self-consistent phonon calculations of lattice dynamical properties in cubic $SrTiO_3$ with first-principles anharmonic force constants, Phys. Rev. B **92**, 054301 (2015).
[24] Y. Xia, V. I. Hegde, K. Pal, X. Hua, D. Gaines, S. Patel, J. He, M. Aykol, and C. Wolverton, High-throughput study of lattice thermal conductivity in binary rocksalt and zinc blende compounds including higher-order anharmonicity, Phys. Rev. X **10**, 041029 (2020).
[25] Z. Tong, X. Yang, T. Feng, H. Bao, and X. Ruan, First-principles predictions of temperature-dependent infrared dielectric function of polar materials by including four-phonon scattering and phonon frequency shift, Phys. Rev. B **101**, 125416 (2020).
[26] M. Simoncelli, N. Marzari, and F. Mauri, Unified theory of thermal transport in crystals and glasses, Nat. Phys. **15**, 809 (2019).
[27] Z. Fan, H. Dong, A. Harju, and T. Ala-Nissila, Homogeneous nonequilibrium molecular dynamics method for heat transport and spectral decomposition with many-body potentials, Phys. Rev. B **99**, 064308 (2019).
[28] D. J. Evans, Homogeneous NEMD algorithm for thermal conductivity–Application of non-canonical linear response theory, Phys. Lett. A **91**, 457 (1982).
[29] A. J. Gabourie, Z. Fan, T. Ala-Nissila, and E. Pop, Spectral decomposition of thermal conductivity: Comparing velocity decomposition methods in homogeneous molecular dynamics simulations, Phys. Rev. B **103**, 205421 (2021).
[30] J. Zheng, D. Shi, Y. Yang, C. Lin, H. Huang, R. Guo, and B. Huang, Anharmonicity-induced phonon hardening and phonon transport enhancement in crystalline perovskite $BaZrO_3$, Phys. Rev. B **105**, 224303 (2022).
[31] X. Wang, Z. Gao, G. Zhu, J. Ren, L. Hu, J. Sun, X. Ding, Y. Xia, and B. Li, Role of high-order anharmonicity and off-diagonal terms in thermal conductivity: A case study of multiphase $CsPbBr_3$, Phys. Rev. B **107**, 214308 (2023).
[32] M. Feng, X. Wang, G. Zhu, C. He, J. Sun, X. Ding, J. Shiomi, Y. Xia, B. Li, and Z. Gao, The relation between the atomic mass ratio and quartic anharmonicity in alkali metal hydrides, Mater. Today Phys. **44**, 101423 (2024).
[33] X. Wang, M. Li, M. Feng, X. Li, Y. Hao, W. Shi, J. He, X. Ding, and Z. Gao, Bonding hierarchy and coordination interaction leading to high thermoelectricity in wide bandgap $TlAgI_2$, Phys. Rev. Mater. **8**, 094601 (2024).
[34] W. Li and N. Mingo, Ultralow lattice thermal conductivity of the fully filled skutterudite $YbFe_4Sb_{12}$ due to the flat avoided-crossing filler modes, Phys. Rev. B **91**, 144304 (2015).
[35] J. Zheng, D. Shi, S. Liu, Y. Yang, C. Lin, Z. Chang, R. Guo, and B. Huang, Effects of high-order anharmonicity on anomalous lattice dynamics and thermal transport in fully filled skutterudite $YbFe_4Sb_{12}$, Phys. Rev. Mater. **6**, 093801 (2022).
[36] Y. Wang, Z. Gao, X. Wang, J. Sun, M. Feng, Y. Hao, X. Li, Y. Zhao, and X. Ding, Anomalous thermal conductivity in 2D silica nanocages of immobilizing noble gas atom, Appl. Phys. Lett. **124**, 122205 (2024).
[37] See Supplemental Material http://link.aps.org/supplemental/10.1103/PhysRevB.111.195207 for the details of applying NEP to calculate force constants for accurate thermal transport modeling in $CuBiSeCl_2$; energy per atom and atomic force of NEP compared with DFT; the comparation of phonon spectra from NEP and DFT calculations; the spectral and cumulative κ_p of $CuBiSeCl_2$ at full frequency range; formulations and results of κ_L for vacancy and grain boundary scattering rates affecting lattice thermal conductivity; n-grid convergence test results of κ_p; κ_p of $CuBiSeCl_2$ with linear scale; projected phonon density of states compared with the phonon scattering rates; potential energy per atom along the *b*-axis direction with quartic and quadratic polynomial fitting; crystal structure of $CuBiSeCl_2$, which also contains Refs. [16–18,21–22,27–29,31–32,36,45,54–55].
[38] Z. Gao, F. Tao, and J. Ren, Unusually low thermal conductivity of atomically thin 2D tellurium, Nanoscale **10**, 12997 (2018).
[39] Y. Hao, Y. Zuo, J. Zheng, W. Hou, H. Gu, X. Wang, X. Li, J. Sun, X. Ding, and Z. Gao, Machine learning for predicting ultralow thermal conductivity and high ZT in complex thermoelectric materials, ACS Appl. Mater. Interfaces **16**, 47866 (2024).
[40] S. Thakur and A. Giri, Origin of ultralow thermal conductivity in metal halide perovskites, ACS Appl. Mater. Interfaces **15**, 26755 (2023).
[41] H. Liu, X. Shi, F. Xu, L. Zhang, W. Zhang, L. Chen, Q. Li, C. Uher, T. Day, and J. Snyder, Copper ion liquid-like thermoelectrics, Nat. Mater. **11**, 422 (2012).
[42] A. S. Pashinkin, M. S. Mikhailova, A. S. Malkova, and V. A. Fedorov, Heat capacity and thermodynamic properties of lead selenide and lead telluride, Inorg. Mater. **45**, 1226 (2009).
[43] Z. Tian, J. Garg, K. Esfarjani, T. Shiga, J. Shiomi, and G. Chen, Phonon conduction in PbSe, PbTe, and $PbTe_{1-x}Se_x$ from first-principles calculations, Phys. Rev. B **85**, 184303 (2012).
[44] Q. D. Gibson, T. Zhao, L. M. Daniels, H. C. Walker, R. Daou, S. Hébert, M. Zanella, M. S. Dyer, J. B. Claridge, B. Slater, M. W. Gaultois, F. Corá, J. Alaria, and M. J. Rosseinsky, Low thermal conductivity in a modular inorganic material with bonding anisotropy and mismatch, Science **373**, 1017 (2021).
[45] Z. Tong, A. Pecchia, C. Yam, T. Dumitrică, and T. Frauenheim, Glass-like transport dominates ultralow lattice thermal conductivity in modular crystalline $Bi_4O_4SeCl_2$, Nano Lett. **23**, 9468 (2023).
[46] G. A. Slack, The thermal conductivity of nonmetallic crystals, Solid State Phys. **34**, 1 (1979).
[47] M. Simoncelli, N. Marzari, and F. Mauri, Wigner formulation of thermal transport in solids, Phys. Rev. X **12**, 041011 (2022).

[48] J. Zheng, C. Lin, C. Lin, G. Hautier, R. Guo, B. Huang, Unravelling ultralow thermal conductivity in perovskite $Cs_2AgBiBr_6$: Dominant wave-like phonon tunnelling and strong anharmonicity, npj Comput. Mater. **10**, 30 (2024).

[49] L. Isaeva, G. Barbalinardo, D. Donadio, and S. Baroni, Modeling heat transport in crystals and glasses from a unified lattice-dynamical approach, Nat. Commun. **10**, 3853 (2019).

[50] X. Wang, M. Feng, Y. Xia, J. Sun, X. Ding, B. Li, and Z. Gao, Revisiting lattice thermal conductivity of CsCl: The crucial role of quartic anharmonicity, Appl. Phys. Lett. **124**, 172201 (2024).

[51] Y. Xia, V. Ozoliņš, and C. Wolverton, Microscopic mechanisms of glasslike lattice thermal transport in cubic $Cu_{12}Sb_4S_{13}$ tetrahedrites, Phys. Rev. Lett. **125**, 085901 (2020).

[52] Y. He, L. Matei, H. J. Jung, K. M. McCall, M. Chen, C. C. Stoumpos, Z. Liu, J. A. Peters, D. Y. Chung, B. W. Wessels, M. R. Wasielewski, V. P. Dravid, A. Burger, and M. G. Kanatzidis, High spectral resolution of gamma-rays at room temperature by perovskite $CsPbBr_3$ single crystals, Nat. Commun. **9**, 1609 (2018).

[53] X. Shen, N. Ouyang, Y. Huang, Y.-H. Tung, C.-C. Yang, M. Faizan, N. Perez, R. He, A. Sotnikov, K. Willa, C. Wang, Y. Chen, and E. Guilmeau, Amorphous-like ultralow thermal transport in crystalline argyrodite Cu_7PS_6, Adv. Sci. **11**, 2400258 (2024).

[54] J. Tiwari and T. Feng, Intrinsic thermal conductivity of ZrC from low to ultrahigh temperatures: A critical revisit, Phys. Rev. Mater. **7**, 065001 (2023).

[55] B. Mortazavi, E. V. Podryabinkin, I. S. Novikov, T. Rabczuk, X. Zhuang, and A. V. Shapeev, Accelerating first-principles estimation of thermal conductivity by machine-learning interatomic potentials: A MTP/ShengBTE solution, Comput. Phys. Commun. **258**, 107583 (2021).

[56] R. Cao, Q.-L. Yang, H.-X. Deng, S.-H. Wei, J. Robertson, and J.-W. Luo, Softening of the optical phonon by reduced interatomic bonding strength without depolarization, Nature (London) **634**, 1080 (2024).

[57] P.-F. Liu *et al.*, Strong low-energy rattling modes enabled liquid-like ultralow thermal conductivity in a well-ordered solid, Nat. Sci. Rev. **11**, nwae216 (2024)